Author Manuscript
Author Manuscript
Author Manuscript
Author Manuscript

HHS Public Access
Author manuscript
Biochemistry. Author manuscript; available in PMC 2019 May 20.

Published in final edited form as:
Biochemistry. 2019 February 12; 58(6): 534–545. doi:10.1021/acs.biochem.8b01044.

Molecular architecture of the inositol phosphatase Siw14

Tyler J. Florio[†], **Ravi K. Lokareddy**[†], **Richard E. Gillilan**[§], and **Gino Cingolani**[†,¥,*]

[†]Dept. of Biochemistry and Molecular Biology, Thomas Jefferson University, 233 South 10th Street, Philadelphia, PA 19107

[§]Macromolecular Diffraction Facility, Cornell High Energy Synchrotron Source (MacCHESS), Cornell University, 161 Synchrotron Drive, Ithaca, NY 14853, USA

[¥]Institute of Biomembranes and Bioenergetics, National Research Council, Via Amendola 165/A, 70126 Bari, Italy

Abstract

Siw14 is a recently discovered inositol phosphatase implicated in suppressing prion propagation in *Saccharomyces cerevisiae*. In this paper, we used hybrid structural methods to decipher Siw14 molecular architecture. We found the protein exists in solution as an elongate monomer ~140 Å in length, containing an acidic N-terminal domain (NTD) and a basic C-terminal dual specificity phosphatase (DSP) domain, structurally similar to the glycogen phosphatase laforin. The two domains are connected by a protease susceptible linker and do not interact *in vitro*. The crystal structure of Siw14-DSP reveals a highly basic phosphate-binding loop and a ~10 Å deep substrate-binding crevice evolved to dephosphorylate pyro-phosphate moieties. A pseudo-atomic model of the full-length phosphatase generated from solution, crystallographic, biochemical and modeling data sheds light on the interesting zwitterionic nature of Siw14, which we hypothesized may play a role in discriminating negatively charged inositol phosphates.

Graphical Abstract

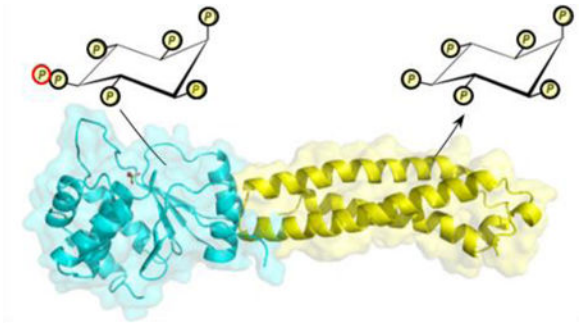

[*]**Corresponding Author** gino.cingolani@jefferson.edu.

Author Contributions

TF, with the help of RL, carried out all steps of data collection, analysis, conceptualization, and figure preparation. GC contributed to the crystallographic methods and RG helped with bioSAXS data collection and analysis. The manuscript was written through the contributions of all authors. All authors have given approval to the final version of the manuscript.

The authors declare no competing financial interests.

Author Manuscript Author Manuscript Author Manuscript Author Manuscript

Keywords

Siw14; dual specificity phosphoprotein phosphatase; inositol phosphate; phosphorylation

INTRODUCTION

Dual-specificity phosphatases (DSPs) are vital signaling molecules first identified in viruses and then found in all kingdoms of life (1, 2). The definition of 'dual-specificity' was inspired by their hydrolytic activity toward both phospho-Tyr (P-Tyr) and phospho-Ser/Thr containing substrates. Vaccinia virus H1 open reading frame, VH1, the first identified DSP (3), is also considered the prototype of this family of phosphatases (2, 4). The human genome encodes 38 VH1-like DSPs (or 'DUSPs' (1)), which control vital signaling pathways and are implicated in a multitude of processes that lead to human diseases (5, 6). A subgroup of 19 human VH1-like phosphatases that lack an N-terminal Cdc25 homology domain is also known as 'atypical' DSPs (7). Atypical DSPs present broad substrate specificity and evolved to dephosphorylate either peptidic or non-peptidic substrates. Well-characterized atypical DSPs include laforin, which dephosphorylates phospho-glycogen (8), the mitochondrial phosphatase PTPMT1 that dephosphorylates phosphatidyl-glycerol phosphate (9), PTEN-like DSPs that are specific to D3-inositol phospholipids (10) and the RNA phosphatase PIR1 (11).

Siw14 (also known as Oca3) is a recently discovered phosphatase that modulates inositol pyrophosphate (PP-IP) metabolism in Saccharomyces cerevisiae. Initial studies found that Siw14 has a negligible affinity toward P-Tyr, but hydrolyzes phosphatidylinositol 3,5-bisphosphate (12). *In vitro* studies using recombinant Siw14 later clarified that Siw14 selectively hydrolyzes the β-phosphate at the 5-position on 5-diphosphoinositol pentakisphosphate (5-PP-IP5) (13). Siw14 is also active toward other PP-IPs such as 5-PP-IP4, 5-IP7 and 1,5-PP-IP4 (also known as IP8), but it has negligible activity against 1-IP7, which is present in very small quantities in yeast cells (14). Thus, the presence of a 5-β-phosphate is an essential determinant for Siw14 catalytic specificity. Yeast strains lacking Siw14 (siw14Δ) have increased 5-PP-IP5 and 1,5-PP-IP4 levels, which can be rescued by heterologous Siw14 (13). Siw14 also plays a role in the organization of the actin cytoskeleton and siw14Δ mutants present actin clumps and cytoskeletal defects during stationary phase (15). Siw14Δ strains also exhibit caffeine sensitivity, which is likely explained by its role in repressing the nuclear localization of Gln3 (16) via the PP2A–Tpd3 complexes (17). In addition, Siw14 functions as a prion-suppressing factor in Saccharomyces cerevisiae possibly due to its phosphatase activity (18) against PP-IPs, which are signal transduction molecules involved in prion propagation (19).

In this paper, we used hybrid structural methods to determine the three-dimensional (3D) organization of yeast Siw14 and shed light on the mechanisms and regulation of inositol phosphatase activity.

Author Manuscript Author Manuscript Author Manuscript Author Manuscript

MATERIALS AND METHODS

Molecular biology techniques.

The gene encoding the full- length Siw14 (FL-Siw14) (res. 1–281) was amplified from *S. cerevisiae* genomic DNA using PCR and cloned in vector pGEX-6P (plasmid pGEX-FL-Siw14). Siw14-DSP (res. 109–281) was subcloned using PCR (plasmid pGEX-Siw14-DSP). Siw14-NTD (res. 1–115) was generated by introducing a stop codon at position 116 (plasmid pGEX-Siw14-NTD). Catalytically inactive Siw14 (with Cys214 mutated to Ser) was generated by site-directed mutagenesis. All plasmids were sequenced to confirm the fidelity of the DNA sequence.

Biochemical techniques.

FL-Siw14 and Siw14-NTD were expressed in *E. coli* strain BL21 (DE3) AI by inducing at 30° C for 4 hours with 0.1 mM IPTG and 0.2% (w/v) arabinose. Cell pellets were dissolved in Lysis Buffer 1 containing 20 mM Tris-HCl pH 8.0, 300 mM NaCl, 1 mM PMSF, 5 mM β-Mercaptoethanol, 0.1% Tween 20 and disrupted by sonication. Recombinant FL-Siw14 and Siw14-NTD were purified on glutathione beads (Gold Biotechnology), cleaved off on beads by overnight digestion with PreScission Protease, and further purified by SEC on a Superdex 200 16/60 (for FL-Siw14) equilibrated with GF1 (20 mM Tris-HCl 8.0, 150 mM NaCl, 5 mM β-Mercaptoethanol) or 75 16/60 (for Siw14-NTD) column (GE Healthcare) equilibrated in CD-buffer (20 mM Na phosphate pH 7.4, 50 mM NaCl). Siw14-DSP was expressed in *E. coli* strain BL21 (DE3) by inducing at 21° C for 12–16 hours with 1 mM IPTG. Cell pellets were dissolved in Lysis Buffer 2 containing 20 mM Tris pH 7.0, 200 mM NaCl, 1 mM EDTA, 1 mM PMSF, 2 mM β-Mercaptoethanol, 0.1% Tween 20 and disrupted by sonication. Recombinant protein was purified on glutathione beads (Gold Biotechnology) and eluted from beads with 15 mM reduced glutathione. GST was cleaved off with PreScission Protease and further purified by SEC on Superdex 75 10/300 column (GE Healthcare) in GF2-buffer (20 mM Tris pH 7.0, 150 mM NaCl, 2 mM β-Mercaptoethanol). Limited proteolysis was performed by adding chymotrypsin to FL-Siw14 in a ratio ~1:200 (w/w), and incubating samples at 22°C and 4°C for 60 minutes. Samples were taken after 5, 10, 15, 30, 45 and 60 minutes, the reaction blocked with 1 mM PMSF and samples analyzed by SDS-PAGE. For pull-down assay, a 3-fold molar excess of purified Siw14-DSP was incubated with beads coupled to GST-NTD, or free GST. After washing 3 times with GF1-buffer bound fraction were analyzed by SDS-PAGE.

In solution biophysical methods.

Circular dichroism (CD) spectra were recorded in the far-UV region (190–260 nm) using a Jasco J-810 spectropolarimeter equipped with a Neslab RTE7 refrigerated recirculator. Siw14-NTD was dissolved at a final concentration of 10 μM (corresponding to 0.3 mg ml^{-1}) in 20 mM Na phosphate (pH 7.4), 50 mM NaCl and analyzed in a rectangular quartz cuvette (Starna Cells, Inc.) with a path length of 0.1 cm. TFE was added to a 20% (v/v) final concentration to stabilize α-helical content (20, 21). AUC-SV analysis was carried out in a Beckman XL-A Analytical Ultracentrifuge. FL-Siw14 samples were dissolved at 15 μM and 50 μM (corresponding to 0.5 and 1.7 mg ml^{-1}) in 20 mM HEPES pH 7.5, 150 mM NaCl, 0.5

Author Manuscript Author Manuscript Author Manuscript Author Manuscript

mM TCEP and were spun at 50,000 rpm at 4° C. Absorbance values at 285 nm were fit to a continuous sedimentation coefficient (c(s)) distribution model in SEDFIT (22).

Crystallographic methods.

Catalytically inactive Siw14-DSP concentrated to 6 mg ml^{-1} was crystallized at 22 °C using the hanging drop vapor diffusion method in the presence of 0.2 M magnesium chloride, 0.1 M HEPES pH 7.5, 17–25% (w/v) PEG3350 in 1:1 drop ratio. Crystals were cryoprotected with 30% ethylene glycol, flash-frozen in liquid nitrogen and diffracted at beam-line 9–2 at the Stanford Synchrotron Radiation Lightsource (SSRL). Complete data to 2.5 Å resolution were collected on a PILATUS 6M Detector. All steps of data indexing, integration and reduction were carried out using HKL2000 (23) and CCP4 programs (24), and the data collection statistics tabulated in Table 1.

The structure was solved by molecular replacement (MR) using the Arabidopsis Thaliana phosphatase At1g05000 (PDB 2q47) (~60% sequence identity) as a search model. Structure determination was complicated by the ambiguity in the space group determination and the unusually high number of copies in the AU. The initial merging of the diffraction data in hexagonal space group ($P6_1$) gave a satisfactory Rsym (~11%), with an estimated six to 12 protein molecules in the AU, based on the solvent-content analysis. However, no satisfactory MR solution was found using At1g05000 as a search model. To overcome this problem (25), exhaustive MR searches were carried out in space group P_1 using MOLREP (26), which identified 48 copies of Siw14-DSP arranged in parallel super-helixes of staggered hexamers. Structure factors calculated from this solution were examined for evidence of symmetry using POINTLESS (27) and Xtriage (28), which suggested the true space group of the data is C2. After reprocessing the diffraction in the correct C2 symmetry, we were able to readily locate 24 copies of Siw14-DSP in the AU, which yielded an unambiguous likelihood score LLG=10,900 using PHASER (29). Xtriage (28), a program in the PHENIX crystallographic software, confirmed the data suffer from pseudo-merohedral twinning with an estimated twinning fraction α=0.35. In C2, 24 copies of Siw14-DSP (each bound to a sulfate ion) assemble in the asymmetric unit (ASU) as four hexameric rings. The ASU content was then subjected to several cycles of manual rebuilding using COOT (30) followed by positional and isotropic B-factor refinement in Phenix (31) using 24-fold non-crystallographic symmetry torsion restraints and including a twinning operator (h, -k, -l). The final model has a R_{work}/R_{free} of 22.98 / 24.63 % using all data between 15–2.50 Å resolution. Final stereochemistry was validated using MolProbity (32) (Table 1).

SAXS analysis.

SEC-SAXS of FL-Siw14 was done at G1 station at MacCHESS, which is equipped with an AKTA Pure FPLC system (GE Healthcare). FL-Siw14 was loaded at 7.2 mg ml^{-1} on a Superdex 200 10/300 GL column (GE Healthcare) equilibrated in 20 mM Tris-HCl pH 7.5, 150 mM NaCl, and 5 mM β-Mercaptoethanol. SAXS data were recorded on a Pilatus 100K-S detector at 2 s per frame with a fixed camera length of 1.522 m and 9.91 keV energy allowing the collection of the angular range q between 0.01–0.27 Å-1. Primary reduction of the SAXS data was performed using RAW (33), and ATSAS software (34). To minimize the effects of damaged material accumulating on the X-ray sample window, the buffer profile

Author Manuscript Author Manuscript Author Manuscript Author Manuscript

was constructed by averaging frames both before (469–525) and after (762–862) the sample peak (575–613). A Guinier plot of the subtracted profile was linear to the lowest measured q value. (35). GNOM (36) was used to calculate *P(r)* plots from the scattering data. The maximum diameter, Dmax = 141 Å, was chosen so that the *P(r)* function fell gradually to zero at r = Dmax unconstrained. The Porod exponent was computed using the program ScÅtter (37). *Ab initio* model calculations to generate an average electron density from solution scattering data were done using DENSS (38) and EMAN2 (39, 40), as implemented in RAW (33). Docking of PDB models inside the SAXS density was done manually and improved by rigid body refinement using Chimera (41) and phenix.real_space_refine (42). Theoretical solution scattering curves were calculated using the FoXS web server (43) and CRYSOL (44). The $\chi 2$ between FL-Siw14 SAXS electron density and the atomic models of DSP and NTD docked in the SAXS density is $\chi 2 = 3.5$, which improved to $\chi 2 = 1.7$ after rigid body-refinement. SEC-SAXS data collection and analysis statistics are in Table 2.

Structure analysis.

Secondary structure prediction of Siw14-NTD was done with JPred4 (45). A *de novo* 3D-model of Siw14-NTD was predicted using the Robetta server (46). The percentage of α-helical content in Siw14-NTD was calculated from ellipticity data using the K2D2 server (47). Structural neighbors of Siw14-DSP were identified using the DALI server (48). The topological diagram in Fig. 3 was generated using PDBsum (49) and secondary structure superimpositions were carried out in Coot (30). All ribbon diagrams and surface representations were prepared using the program Pymol (50) and Chimera (41). Non-linear Poisson-Boltzmann electrostatic calculations were performed using APBS Tools (51).

RESULTS

Siw14 contains two domains.

FL-Siw14 consists of 281 residues and has predicted M.W. of 32,755 Da. It contains a C-terminal DSP domain (res. 117–281) enriched in basic amino acids (isoelectric point 9.0) (14) preceded by a very acidic NTD (res. 1–108, isoelectric point 4.4) (Fig. 1A).

To interrogate the conformational flexibility of FL-Siw14, we subjected the purified protein to limited proteolysis in the presence of chymotrypsin (Fig. 1B). This treatment yielded two fragments of ~18 kDa and ~13 kDa that formed within the first 5 minutes of digestion and remained stable over time, both at 4 and 22 °C. Mass spectrometry analysis and N-terminal sequencing identified a chymotrypsin cleavage site between residues Leu-108/Asn-109, suggesting the 18 kDa band seen on gel corresponds to the C-terminal DSP domain and the smaller ~13 kDa species is Siw14-NTD. Aiming at structural studies, we subcloned and purified milligram-quantities of both NTD and DSP from soluble bacterial extracts. Despite the very different charge, the two domains failed to form a complex in a pull-down assay carried out at micromolar concentrations (Fig. 1C). Thus, Siw14 contains two domains connected by a protease susceptible linker. The linker is susceptible to proteolysis after only 5 min at 4° C, as well as the isolated NTD and DSP, do not appear to interact with each other, suggesting a bead-on-a-string topology.

Author Manuscript Author Manuscript Author Manuscript Author Manuscript

Siw14-NTD is enriched in α-helices.

The amino acid sequence of Siw14-NTD lacks obviously recognizable similarity to known proteins. Secondary structure prediction suggests that as many as 80 residues of Siw14-NTD have a propensity to adopt a α-helical fold, while the N-terminal 15 residues are likely unstructured (Fig. 2A).

Jpred4 (43) and Robetta (46) folds Siw14-NTD into a three-helix bundle with a partially disordered N-terminal tail. We used far-UV circular dichroism (CD) to investigate the secondary structure content of Siw14-NTD in solution. Spectra recorded at neutral pH using 10 μM final concentration of Siw14-NTD revealed a predominantly unstructured conformation (Fig. 2B), possibly consistent with a mixture of secondary structures and random coil. However, α-helix content was induced by the addition of 20% 2,2,2-trifluoroethanol (TFE), a kosmotropic (order inducing) compound known to stabilize α-helical content (20, 21). This folded conformation of Siw14-NTD was revealed by the appearance of two minima in the ellipticity at 222 and 208 nm and a maximum at 195 nm (Fig. 2B). The helical content observed in the presence of TFE was estimated to be about 88% of NTD sequence, in a good agreement with the predicted secondary structure content (Fig. 2A). Thus, Siw14-NTD has a propensity to adopt a folded structure enriched in α-helices, which is triggered *in vitro* by TFE and is possibly stabilized *in vivo* by the highly proteinaceous environment of living cells (52).

Crystal structure of catalytically inactive Siw14-DSP.

Since Siw14 failed to crystallize as a FL protein, we generated a catalytically inactive Siw14-DSP core by replacing the active site Cys-214 with Ser (13). This less reactive DSP yielded crystals diffracting X-rays beyond 2.5 Å resolution (Table 1). The structure of Siw14-DSP was solved by molecular replacement and refined to an $R_{work}/_{free}$ of 22.98 / 24.63 %. The ASU contains 24 copies of Siw14-DSP, each bound to a sulfate ion, assembled as four hexameric rings built by stacked trimers of Siw14-DSP (Fig. S1). This oligomeric state is likely a crystallographic packing artifact, as the DSP core is strictly monomeric in solution (14).

Siw14-DSP adopts a quasi-globular structure of 45×35×60 Å, with N- and C-termini projecting in opposite directions (Fig. 3A).

It presents the classical topology of VH1-like DSPs (53), built by a central five-stranded β-sheet (β1-β5) (highlighted in light blue in Fig. 3B) sandwiched between two clusters of α-helices, eight in the case of Siw14, that make contacts with the solvent (named h1-h2 and h3-h8 in Fig. 3A, B). Siw14 ‘general acid loop’ (or ‘WPD-loop’, res. 179–192), invisible in a previous structure (14), was resolved in our structure by computing a 24-fold noncrystallographic symmetry averaged electron density map. Superimposition of all 24 chains present in the ASU suggests a global RMSD of 1.07 Å for all atoms and 0.38 Å for alpha carbons (Fig. S2). Chain S is the most dissimilar from the reference chain A, with global RMSD of 2.12 Å (RMSD for alpha carbon is 1.72 Å). This long loop has an averaged B-factor of ~85.1 A^2 higher than the rest of the protein atoms (~55.8 A^2, Table 1) and shows significant differences in the 24 copies in the ASU with global RMSD of 1.45 Å (Fig. S2).

Author Manuscript Author Manuscript Author Manuscript Author Manuscript

In the structure, the WPD-loop forms a ridge that surrounds the active site generating a remarkably deep active site cleft.

Siw14 catalytic triad (Fig. 3C) consists of Cys-214 (the catalytic residue), Arg-220 (the general base) and Glu-185 (the general acid): the first two residues are part of a phosphate-binding loop, or 'PTP-loop' (res. 214–220), while Glu-185 is located in the 'WPD-loop' (res. 179–191) (Fig. 3B). Superimposition of the 24 copies of Siw14-DSPs in the ASU reveals the side chain of Arg-216 is highly flexible and can adopt different conformations (Fig. 3C). In two-thirds of the copies in the ASU, Arg-216 surrounds the sulfate ion, adopting a conformation similar to that seen in Siw14 complex with citrate (14). In eight of the 24 copies, the side chain of Arg-216 is in an open conformation that swings away from the active site sulfur to make a bidentate contact with Glu-120. Interesting, Ala-mutation of Arg-216 reduces Siw14's Kcat/Km by 58%, suggesting a direct involvement of this residue in catalysis (14). Overall, the presence of four basic residues in Siw14 PTP-loop (Arg-216, Lys-218, His-202, and Arg-220) makes the active site pocket deep, burying the catalytic Cys-214 ~10 Å below the enzyme surface (also shown in Fig. 4B). This is comparable to the active site groove of PIR1, an RNA phosphatase that also dephosphorylates pyro-phosphate (54).

Structural similarity to laforin.

A DALI search (48) found that Siw14-DSP bears structural similarity to several atypical DSPs including the glucan phosphatase laforin (Z-score = 13.6) (55), which superimposes to Siw14-DSP with RMSD of 2.8 Å. A structure-based sequence alignment of laforin and Siw14 DSPs is in Fig. S3, while figures 4A and S4 show a side-by-side comparison of Siw14 and laforin DSP (laf-DSP) highlighting the position of critical loops surrounding the active site.

Siw14-DSP presents three noticeable differences from laf-DSP: first, a different number and arrangement of α-helices surrounding the β-sheet core: only two α-helices below the β-sheet core for Siw14 (Fig. 4A) versus four in laforin. Siw14 has an additional C-terminal α-helix (h8) (res. 265–263) (colored in red in Fig. 3B) orthogonal to helix 7, which makes contacts to the central β-sheets via a C-terminal extension (res. 275–281). Second, Siw14 WPD-loop, which usually harbors the general acid residue important for acid-base catalysis (56), is significantly longer than in laforin (13 versus nine residues) (53) (Fig. 4A). Here a glutamate residue (Glu-185) replaces a more common aspartate, although mutational analysis found this residue is important, but not essential for catalytic activity toward 5-IP7 *in vitro* (14). Third, Siw14 active site cleft is remarkably deeper than in laforin (Fig. 4B,C) (53) mainly due to the presence of long side-chains in the PTP-loop and because of the conformation and length of the WPD-loop that surrounds the active site. Siw14 catalytic residue Cys-214 sits at bottom of this deep crevice, buried ~10 Å below the enzyme surface. The distance between Cys-214 and the general acid Glu-185 is as much as 20 Å in our crystal structure.

Author Manuscript Author Manuscript Author Manuscript Author Manuscript

Biophysical analysis of FL-Siw14.

To shed light on the structure of the FL-Siw14, we carried out size exclusion chromatography (SEC) coupled with small angle X-ray scattering (SEC-SAXS) at a concentration of 7.2 mg ml^{-1} (Fig. 5A).

This technique is well suited to separate aggregates from monodisperse species, allowing for accurate SAXS analysis from samples prone to aggregation (57). SEC-SAXS revealed a radius of gyration (R_g) of 33.3 + 0.3 Å (Fig. 5B, Table 2). The distance distribution function *P(r)* calculated from SAXS data indicates an extended molecule (maximum diameter, Dmax ~141 Å), with a major peak at 25 Å (Fig. 5C). The Porod mass calculated from SAXS data is ~34.2 kDa, also consistent with a monomer of Siw14 (M.W. ~32.7 kDa). The normalized Kratky plot has a peak at qRg = 3.0 > √3 indicating non-globular shape, but also falls to zero consistent with a folded structure (Fig. 5D) (58). The Porod exponent power law fit gives p = 3.0 indicating the full-length structure is not completely rigid.

SEC-SAXS was validated using analytical ultracentrifugation (AUC) operated under sedimentation velocity (SV) mode (Fig. 5E). At 1.7 mg ml^{-1}, FL-Siw14 migrated as a homogeneous species characterized by a monophasic sedimentation boundary indicative of a single major (>95.2%) component in solution migrating with an apparent sedimentation coefficient (s*) of 1.39S (Fig. 5F, Table 2). Conversion of the distribution of the apparent sedimentation coefficient to molecular mass revealed an M.W. ~31.0 kDa, in good agreement with the Porod mass calculated from SAXS data (~33.9 kDa). The frictional ratio obtained from sedimentation measurements (*f/fo*) is ~2.5 (Table 2), indicative of an elongated molecule. Thus, both SEC-SAXS and AUC-SV describe FL-Siw14 as an elongate and well-folded monomeric protein.

A *pseudo*-atomic model of FL-Siw14.

To visualize the structural organization of the FL-Siw14, we calculated an electron density from solution scattering data (Table 2). The average electron density has an estimated resolution of 27 Å (by Fourier Shell Correlation), as reported by DENSS (38). The SAXS electron density is shaped like a ‘pestle’, with a tapered and a bulgy lobe, spanning about 140 Å in length (Fig. 6A).

The larger lobe accommodates Siw14-DSP with remarkable accuracy, with the N-terminus projecting toward the thinner lobe. The rest of density fits well to a *de novo* model of Siw14-NTD that is predicted to fold into a three-helix bundle. Overall, Siw14-NTD is positioned distal from the DSP, and the linker between DSP and NTD is protease sensitive (in red in Fig. 6A), consistent with the observed susceptibility to chymotrypsin (Fig. 2B). The complete pseudo-atomic model of FL-Siw14 was subjected to rigid-body refinement against the SAXS density yielding a final model that has excellent agreement with the experimental SAXS data (χ^2 =1.7) (Fig. 6B). A surface potential representation reveals the zwitterionic nature of FL-Siw14, which is highly basic in the DSP, mainly around the active site, but exposes considerable acidic charge in the NTD (Fig. 6C).

Author Manuscript Author Manuscript Author Manuscript Author Manuscript

DISCUSSION

The DSP domain is conserved in all kingdoms of life where it evolved to dephosphorylate both peptidic and non-peptidic substrates. Though the minimal catalytic core of a cysteine-based phosphatase is ~150 residues (59), several DSPs assemble into functional dimers (e.g. VH1 (53, 60), DUSP27 (61), and laforin (55)) and/or bear regulatory domains in the vicinity of the DSP core important for catalytic activity. For instance, laforin has an N-terminal carbohydrate-binding module (CBM) essential for catalytic activity (55, 62); DUSP1, DUSP2, DUSP6, and DUSP5 contain an N-terminal Cell Division Cycle 25 (CDC25)-homology domain (1); PTEN has a C-terminal C2 domain (63); HCE1 and DUSP12 present a guanylyltransferase domain and a Zn-binding domain, respectively (7). In many cases, extensions longer than 80 residues lacking obviously recognizable domain organization surround the DSP core and are poorly characterized in both structure and regulatory function. Overall, the interplay between DSP and flanking domains is poorly understood.

In this paper, we have derived a complete structural model of Siw14 using hybrid structural methods. We found Siw14 exists as a monomer in solution at physiological concentration, as previously observed for PIR1 (54) and DUSP26 (64). We identified two folded domains in Siw14: a α-helical NTD rich in acidic residues and a C-terminal basic DSP that, together, generate an elongate molecule ~140 Å in length. Spectroscopic studies revealed Siw14-NTD exists in solution as a mixture of secondary structure conformations and random coil, which readily fold into a helical structure (~88% helical content) upon addition of the α-helix inducing solvent TFE. This is similar to the IBB-domain of importin α, which is fully helical in complex with importin β (65, 66), but remains mainly unstructured in solution in the absence of TFE (67). Though the atomic structure of Siw14-NTD is unknown, *de novo* structure prediction using Robetta folds this domain into a helical bundle somewhat similar to the spectrin repeat (68). In parallel, the crystal structure of Siw14-DSP core revealed structural similarity to laforin, a glucan phosphatase that removes phosphate moieties from glycogen. This structural observation is consistent with the chemistry of inositol, which is a carbocyclic sugar like glucose. Unlike laforin, Siw14 presents a deep catalytic pocket similar to the RNA phosphatase PIR1 (54) that also dephosphorylates pyro-phosphates. Siw14 PTP-loop is rich is basic side chains, including Arg-216, which exists in two distinct conformations in our crystal structure. This residue, important for 5-PP-IP4 hydrolysis (14), adopts an open conformation stabilized by a salt bridge with Glu-120 and a closed conformation that narrows down around the active site sulfate. Siw14 general acid Glu-185 sits on top of a very extended flexible loop, invisible in a previous structure (14) and likely to undergo dynamic movement during catalysis (69). Previous mutagenesis studies (14) revealed this residue is important, but not essential for catalysis in Siw14-DSP. This is different from laforin and VH1 that absolutely require a general acid, as well as PTEN (63) and PIR1 (54), whose phosphatase activity is independent of a general acid, possibly because of the low pKa of the leaving group. Interestingly, there is a second acidic residue in Siw14 (Glu-120) positioned at an almost equal distance from the catalytic Cys-214 and the general acid Glu-185 that was found to be important, though not essential, for catalytic activity *in vitro* (14). Future enzymatic studies will have to address if both Glu-120 and Glu-185 are involved in enzymatic activity, possibly acting like an acidic dyad. Finally,

Author Manuscript Author Manuscript Author Manuscript Author Manuscript

Siw14 DSP and NTD do not interact with each other *in vitro*, suggesting the two domains are structurally independent and may adopt a “beads-on-a-string–like” topology. Consistent with this idea, the linker between NTD and DSP is readily cleaved by chymotrypsin in solution. Likewise, the isolated Siw14-DSP domain retains complete catalytic activity *in vitro* (14) in stark contrast to dimeric DSPs like laforin (55) and VH1 (60) that are inactivated by removal of the domain N-terminal of the DSP.

One of the most noticeable findings of this paper is the remarkably zwitterionic nature of Siw14, which is dictated by a very acidic N-terminus and basic C-terminal DSP domain (Fig. 6C, Table S1). We propose the intrinsic dipole in FL-Siw14 plays a biological role and could serve at least three putative functions: (i) Siw14 acidic NTD may harbor a binding site for another factor yet to be identified that possibly interacts with the phosphatase via electrostatic interactions. (ii) Siw14-NTD could function by repelling negatively charged inositol phosphates and thus be involved in substrate specificity and discrimination. (iii) Finally, Siw14 zwitterionic nature may be responsible for suppressing prions in yeast, a function so far ascribed exclusively to Siw14 phosphatase activity against inositol phosphates (18). This idea is supported by the recent finding that zwitterionic polymers inhibit protein aggregation *in vitro* (70). Future functional and *in vivo* studies are now required to validate the proposed role of Siw14-NTD in suppressing prions in yeast. In conclusion, the structure of Siw14 presented in this paper sheds light on a novel inositol phosphatase and reveals how subtle variations on the classical DSP fold affects Siw14 active site conformation and, potentially, substrate specificity.

Supplementary Material

Refer to Web version on PubMed Central for supplementary material.

ACKNOWLEDGMENT

We are thankful to the staff at SSRL station 9:2 for beamtime and assistance in X-ray data collection. We also thank the staff at macCHESS for help with SEC-SAXS data collection and analysis. The content is solely the responsibility of the authors and does not necessarily represent the official views of the National Institutes of Health. The atomic coordinates and structure factors for Siw14-DSP have been deposited in the Protein Data Bank with accession codes **6E3B**.

Funding Sources

This work is supported in part by NIH grants GM122844 and Z82701. Research in this publication includes work carried out at the Kimmel Cancer Center X-ray Crystallography and Molecular Interaction Facility at Thomas Jefferson University, which is supported in part by NCI Cancer Center Support Grant P30 CA56036 and S10.

ABBREVIATIONS

DSP	Dual Specificity Phosphatase
PTP	phosphotyrosine phosphatases
P-Tyr	phospho-Tyr
FL	full length
3D	three-dimensional

Author Manuscript Author Manuscript Author Manuscript Author Manuscript

SEC	size exclusion chromatography
CD	circular dichroism
TFE	2,2,2-trifluoroethanol
SDS-PAGE	sodium dodecyl sulfate polyacrylamide gel electrophoresis
PMSF	phenylmethylsulfonyl fluoride
TCEP	tris(2-carboxyethyl)phosphine
HEPES	(2-hydroxyethyl)-1-piperazineethanesulfonic acid
SSRL	Stanford Synchrotron Radiation Lightsource
laf-DSP	laforin DSP
ASU	asymmetric unit
RMSD	root mean square deviation
AUC	Analytical Ultracentrifugation
SV	sedimentation velocity
s*	sedimentation coefficient
RH	radius of hydration
SAXS	Small Angle X-ray Scattering
$\mathbf{R_g}$	radius of gyration
P(r)	distance distribution function
CBM	Carbohydrate-binding Module

REFERENCES

1. Patterson KI, Brummer T, O'Brien PM, and Daly RJ (2009) Dual-specificity phosphatases: critical regulators with diverse cellular targets, Biochem J 418, 475–489. [PubMed: 19228121]
2. Alonso A, Sasin J, Bottini N, Friedberg I, Osterman A, Godzik A, Hunter T, Dixon J, and Mustelin T (2004) Protein tyrosine phosphatases in the human genome, Cell 117, 699–711. [PubMed: 15186772]
3. Guan KL, Broyles SS, and Dixon JE (1991) A Tyr/Ser protein phosphatase encoded by vaccinia virus, Nature 350, 359–362. [PubMed: 1848923]
4. Zhang ZY (2002) Protein tyrosine phosphatases: structure and function, substrate specificity, and inhibitor development, Annu Rev Pharmacol Toxicol 42, 209–234. [PubMed: 11807171]
5. Ducruet AP, Vogt A, Wipf P, and Lazo JS (2005) Dual specificity protein phosphatases: therapeutic targets for cancer and Alzheimer's disease, Annu Rev Pharmacol Toxicol 45, 725–750. [PubMed: 15822194]
6. Tautz L, Critton DA, and Grotegut S (2013) Protein tyrosine phosphatases: structure, function, and implication in human disease, Methods Mol Biol 1053, 179–221. [PubMed: 23860656]
7. Bayon Y, and Alonso A (2010) Atypical DUSPs: 19 phosphatases in search of a role, Emerging Signaling Pathways in Tumor Biology, 185–208.

Author Manuscript Author Manuscript Author Manuscript Author Manuscript

8. Tagliabracci VS, Turnbull J, Wang W, Girard JM, Zhao X, Skurat AV, Delgado-Escueta AV, Minassian BA, Depaoli-Roach AA, and Roach PJ (2007) Laforin is a glycogen phosphatase, deficiency of which leads to elevated phosphorylation of glycogen in vivo, Proc Natl Acad Sci U S A 104, 19262–19266. [PubMed: 18040046]
9. Xiao J, Engel JL, Zhang J, Chen MJ, Manning G, and Dixon JE (2011) Structural and functional analysis of PTPMT1, a phosphatase required for cardiolipin synthesis, Proc Natl Acad Sci U S A 108, 11860–11865. [PubMed: 21730175]
10. Maehama T, Taylor GS, and Dixon JE (2001) PTEN and myotubularin: novel phosphoinositide phosphatases, Annu Rev Biochem 70, 247–279. [PubMed: 11395408]
11. Yuan Y, Li DM, and Sun H (1998) PIR1, a novel phosphatase that exhibits high affinity to RNA. ribonucleoprotein complexes, J Biol Chem 273, 20347–20353. [PubMed: 9685386]
12. Roma-Mateo C, Rios P, Tabernero L, Attwood TK, and Pulido R (2007) A novel phosphatase family, structurally related to dual-specificity phosphatases, that displays unique amino acid sequence and substrate specificity, J Mol Biol 374, 899–909. [PubMed: 17976645]
13. Steidle EA, Chong LS, Wu M, Crooke E, Fiedler D, Resnick AC, and Rolfes RJ (2016) A Novel Inositol Pyrophosphate Phosphatase in Saccharomyces cerevisiae: Siw14 PROTEIN SELECTIVELY CLEAVES THE beta-PHOSPHATE FROM 5-DIPHOSPHOINOSITOL PENTAKISPHOSPHATE (5PP-IP5), J Biol Chem 291, 6772–6783. [PubMed: 26828065]
14. Wang H, Gu C, Rolfes RJ, Jessen HJ, and Shears SB (2018) Structural and biochemical characterization of Siw14: A protein-tyrosine phosphatase fold that metabolizes inositol pyrophosphates, J Biol Chem 293, 6905–6914. [PubMed: 29540476]
15. Care A, Vousden KA, Binley KM, Radcliffe P, Trevethick J, Mannazzu I, and Sudbery PE (2004) A synthetic lethal screen identifies a role for the cortical actin patch/endocytosis complex in the response to nutrient deprivation in Saccharomyces cerevisiae, Genetics 166, 707–719. [PubMed: 15020461]
16. Hirasaki M, Kaneko Y, and Harashima S (2008) Protein phosphatase Siw14 controls intracellular localization of Gln3 in cooperation with Npr1 kinase in Saccharomyces cerevisiae, Gene 409, 34–43. [PubMed: 18166280]
17. Tate JJ, Georis I, Feller A, Dubois E, and Cooper TG (2009) Rapamycin-induced Gln3 dephosphorylation is insufficient for nuclear localization: Sit4 and PP2A phosphatases are regulated and function differently, J Biol Chem 284, 2522–2534. [PubMed: 19015262]
18. Wickner RB, Kelly AC, Bezsonov EE, and Edskes HK (2017) [PSI+] prion propagation is controlled by inositol polyphosphates, Proc Natl Acad Sci U S A 114, E8402–E8410. [PubMed: 28923943]
19. Wickner RB, Bezsonov EE, Son M, Ducatez M, DeWilde M, and Edskes HK (2018) Anti-Prion Systems in Yeast and Inositol Polyphosphates, Biochemistry 57, 1285–1292. [PubMed: 29377675]
20. Casanova-Morales N, Alavi Z, Wilson CAM, and Zocchi G (2018) Identifying Chaotropic and Kosmotropic Agents by Nanorheology, J Phys Chem B 122, 3754–3759. [PubMed: 29540059]
21. Lokareddy RK, Sankhala RS, Roy A, Afonine PV, Motwani T, Teschke CM, Parent KN, and Cingolani G (2017) Portal protein functions akin to a DNA-sensor that couples genome-packaging to icosahedral capsid maturation, Nat Commun 8, 14310. [PubMed: 28134243]
22. Schuck P (2000) Size-distribution analysis of macromolecules by sedimentation velocity ultracentrifugation and lamm equation modeling, Biophys J 78, 1606–1619. [PubMed: 10692345]
23. Otwinowski Z, and Minor W (1997) Processing of X-ray Diffraction Data Collected in Oscillation Mode, Methods in Enzymology 276, 307–326.
24. (1994) The CCP4 suite: programs for protein crystallography, Acta Crystallogr D Biol Crystallogr 50, 760–763. [PubMed: 15299374]
25. Sliwiak J, Jaskolski M, Dauter Z, McCoy AJ, and Read RJ (2014) Likelihood-based molecular-replacement solution for a highly pathological crystal with tetartohedral twinning and sevenfold translational noncrystallographic symmetry, Acta Crystallogr D Biol Crystallogr 70, 471–480. [PubMed: 24531481]
26. Vagin A, and Teplyakov A (2010) Molecular replacement with MOLREP, Acta Crystallogr D Biol Crystallogr 66, 22–25. [PubMed: 20057045]

Author Manuscript Author Manuscript Author Manuscript Author Manuscript

27. Evans P (2006) Scaling and assessment of data quality, Acta Crystallogr D Biol Crystallogr 62, 72–82. [PubMed: 16369096]
28. Adams PD, Afonine PV, Bunkoczi G, Chen VB, Davis IW, Echols N, Headd JJ, Hung LW, Kapral GJ, Grosse-Kunstleve RW, McCoy AJ, Moriarty NW, Oeffner R, Read RJ, Richardson DC, Richardson JS, Terwilliger TC, and Zwart PH (2004) PHENIX: a comprehensive Python-based system for macromolecular structure solution, Acta Crystallogr D Biol Crystallogr 66, 213–221.
29. McCoy AJ, Grosse-Kunstleve RW, Adams PD, Winn MD, Storoni LC, and Read RJ (2007) Phaser crystallographic software, J Appl Crystallogr 40, 658–674. [PubMed: 19461840]
30. Emsley P, and Cowtan K (2004) Coot: model-building tools for molecular graphics, Acta Crystallogr D Biol Crystallogr 60, 2126–2132. [PubMed: 15572765]
31. Adams PD, Grosse-Kunstleve RW, Hung LW, Ioerger TR, McCoy AJ, Moriarty NW, Read RJ, Sacchettini JC, Sauter NK, and Terwilliger TC (2002) PHENIX: building new software for automated crystallographic structure determination, Acta Crystallogr D Biol Crystallogr 58, 1948–1954. [PubMed: 12393927]
32. Chen VB, Arendall WB 3rd, Headd JJ, Keedy DA, Immormino RM, Kapral GJ, Murray LW, Richardson JS, and Richardson DC (2010) MolProbity: all-atom structure validation for macromolecular crystallography, Acta Crystallogr D Biol Crystallogr 66, 12–21. [PubMed: 20057044]
33. Hopkins JB, Gillilan RE, and Skou S (2017) BioXTAS RAW: improvements to a free open-source program for small-angle X-ray scattering data reduction and analysis, J Appl Crystallogr 50, 1545–1553. [PubMed: 29021737]
34. Franke D, Petoukhov MV, Konarev PV, Panjkovich A, Tuukkanen A, Mertens HDT, Kikhney AG, Hajizadeh NR, Franklin JM, Jeffries CM, and Svergun DI (2017) ATSAS 2.8: a comprehensive data analysis suite for small-angle scattering from macromolecular solutions, J Appl Crystallogr 50, 1212–1225. [PubMed: 28808438]
35. Petoukhov MV, Franke D, Shkumatov AV, Tria G, Kikhney AG, Gajda M, Gorba C, Mertens HD, Konarev PV, and Svergun DI (2012) New developments in the ATSAS program package for small-angle scattering data analysis, J Appl Crystallogr 45, 342–350. [PubMed: 25484842]
36. Svergun DI, Semenyuk AV, and Reigin LA (1988) Small-Angle-Scattering-Data Treatment by the Regularization Method Acta Crystallogr A A44, 244–250.
37. Rambo RP, and Tainer JA (2011) Characterizing flexible and intrinsically unstructured biological macromolecules by SAS using the Porod-Debye law, Biopolymers 95, 559–571. [PubMed: 21509745]
38. Grant TD (2018) Ab initio electron density determination directly from solution scattering data, Nat Methods 15, 191–193. [PubMed: 29377013]
39. Tang G, Peng L, Baldwin PR, Mann DS, Jiang W, Rees I, and Ludtke SJ (2007) EMAN2: an extensible image processing suite for electron microscopy, J Struct Biol 157, 38–46. [PubMed: 16859925]
40. Galaz-Montoya JG, Flanagan J, Schmid MF, and Ludtke SJ (2015) Single particle tomography in EMAN2, J Struct Biol 190, 279–290. [PubMed: 25956334]
41. Pettersen EF, Goddard TD, Huang CC, Couch GS, Greenblatt DM, Meng EC, and Ferrin TE (2004) UCSF Chimera--a visualization system for exploratory research and analysis, J Comput Chem 25, 1605–1612. [PubMed: 15264254]
42. Afonine PV, Headd JJ, Terwilliger TC, and Adams PD (2013) New Tool: phenix.real_space_refine, Computational Crystallography Newsletter 4, 43–44.
43. Schneidman-Duhovny D, Hammel M, and Sali A (2010) FoXS: a web server for rapid computation and fitting of SAXS profiles, Nucleic Acids Res 38, W540–544. [PubMed: 20507903]
44. Svergun DI, Barberato C, and Koch MHJ (1995) CRYSOL – a Program to Evaluate X-ray Solution Scattering of Biological Macromolecules from Atomic Coordinates, J Appl Crystallogr 28, 768–773.
45. Drozdetskiy A, Cole C, Procter J, and Barton GJ (2015) JPred4: a protein secondary structure prediction server, Nucleic Acids Res 43, W389–394. [PubMed: 25883141]
46. Kim DE, Chivian D, and Baker D (2004) Protein structure prediction and analysis using the Robetta server, Nucleic Acids Res 32, W526–531. [PubMed: 15215442]

Author Manuscript Author Manuscript Author Manuscript Author Manuscript

47. Perez-Iratxeta C, and Andrade-Navarro MA (2008) K2D2: estimation of protein secondary structure from circular dichroism spectra, BMC Struct Biol 8, 25. [PubMed: 18477405]
48. Holm L, and Rosenstrom P (2010) Dali server: conservation mapping in 3D, Nucleic Acids Res 38, W545–549. [PubMed: 20457744]
49. Laskowski RA (2009) PDBsum new things, Nucleic Acids Res 37, D355–359. [PubMed: 18996896]
50. The PyMOL Molecular Graphics System, V, Schrödinger, LLC (unpublished19/08/201019/08/2010).
51. Dolinsky TJ, Nielsen JE, McCammon JA, and Baker NA (2004) PDB2PQR: an automated pipeline for the setup of Poisson-Boltzmann electrostatics calculations, Nucleic Acids Res 32, W665–667. [PubMed: 15215472]
52. Mukherjee S, Waegele MM, Chowdhury P, Guo L, and Gai F (2009) Effect of macromolecular crowding on protein folding dynamics at the secondary structure level, J Mol Biol 393, 227–236. [PubMed: 19682997]
53. Koksal AC, Nardozzi JD, and Cingolani G (2009) Dimeric quaternary structure of the prototypical dual specificity phosphatase VH1, J Biol Chem 284, 10129–10137. [PubMed: 19211553]
54. Sankhala RS, Lokareddy RK, and Cingolani G (2014) Structure of Human PIR1, an Atypical Dual-Specificity Phosphatase, Biochemistry 53, 862–871. [PubMed: 24447265]
55. Sankhala RS, Koksal AC, Ho L, Nitschke F, Minassian BA, and Cingolani G (2014) Dimeric quaternary structure of human laforin, J Biol Chem
56. Zhang ZY, Wang Y, and Dixon JE (1994) Dissecting the catalytic mechanism of protein-tyrosine phosphatases, Proc Natl Acad Sci U S A 91, 1624–1627. [PubMed: 8127855]
57. Acerbo AS, Cook MJ, and Gillilan RE (2015) Upgrade of MacCHESS facility for X-ray scattering of biological macromolecules in solution, J Synchrotron Radiat 22, 180–186. [PubMed: 25537607]
58. Rambo RP, and Tainer JA (2013) Super-resolution in solution X-ray scattering and its applications to structural systems biology, Annu Rev Biophys 42, 415–441. [PubMed: 23495971]
59. Alonso A, Burkhalter S, Sasin J, Tautz L, Bogetz J, Huynh H, Bremer MC, Holsinger LJ, Godzik A, and Mustelin T (2004) The minimal essential core of a cysteine-based protein-tyrosine phosphatase revealed by a novel 16-kDa VH1-like phosphatase, VHZ, J Biol Chem 279, 35768–35774. [PubMed: 15201283]
60. Koksal AC, and Cingolani G (2011) Dimerization of Vaccinia virus VH1 is essential for dephosphorylation of STAT1 at tyrosine 701, J Biol Chem 286, 14373–14382. [PubMed: 21362620]
61. Lountos GT, Tropea JE, and Waugh DS (2011) Structure of human dual-specificity phosphatase 27 at 2.38 A resolution, Acta Crystallogr D Biol Crystallogr 67, 471–479. [PubMed: 21543850]
62. Raththagala M, Brewer MK, Parker MW, Sherwood AR, Wong BK, Hsu S, Bridges TM, Paasch BC, Hellman LM, Husodo S, Meekins DA, Taylor AO, Turner BD, Auger KD, Dukhande VV, Chakravarthy S, Sanz P, Woods VL Jr., Li S, Vander Kooi CW, and Gentry MS (2014) Structural mechanism of laforin function in glycogen dephosphorylation and lafora disease, Mol Cell 57, 261–272. [PubMed: 25544560]
63. Lee JO, Yang H, Georgescu MM, Di Cristofano A, Maehama T, Shi Y, Dixon JE, Pandolfi P, and Pavletich NP (1999) Crystal structure of the PTEN tumor suppressor: implications for its phosphoinositide phosphatase activity and membrane association, Cell 99, 323–334. [PubMed: 10555148]
64. Lokareddy RK, Bhardwaj A, and Cingolani G (2013) Atomic structure of dual-specificity phosphatase 26, a novel p53 phosphatase, Biochemistry 52, 938–948. [PubMed: 23298255]
65. Cingolani G, Petosa C, Weis K, and Muller CW (1999) Structure of importin-beta bound to the IBB domain of importin-alpha, Nature 399, 221–229. [PubMed: 10353244]
66. Mitrousis G, Olia AS, Walker-Kopp N, and Cingolani G (2008) Molecular basis for the recognition of snurportin 1 by importin beta, J Biol Chem 283, 7877–7884. [PubMed: 18187419]
67. Cingolani G, Lashuel HA, Gerace L, and Muller CW (2000) Nuclear import factors importin alpha and importin beta undergo mutually induced conformational changes upon association, FEBS Lett 484, 291–298. [PubMed: 11078895]

Author Manuscript Author Manuscript Author Manuscript Author Manuscript

68. Pascual J, Pfuhl M, Rivas G, Pastore A, and Saraste M (1996) The spectrin repeat folds into a three-helix bundle in solution, FEBS Lett 383, 201–207. [PubMed: 8925896]

69. Hu X, and Stebbins CE (2006) Dynamics of the WPD loop of the Yersinia protein tyrosine phosphatase, Biophys J 91, 948–956. [PubMed: 16698773]

70. Rajan R, and Matsumura K (2017) Inhibition of protein aggregation by zwitterionic polymer-based core-shell nanogels, Sci Rep 7, 45777. [PubMed: 28374820]

Author Manuscript Author Manuscript Author Manuscript Author Manuscript

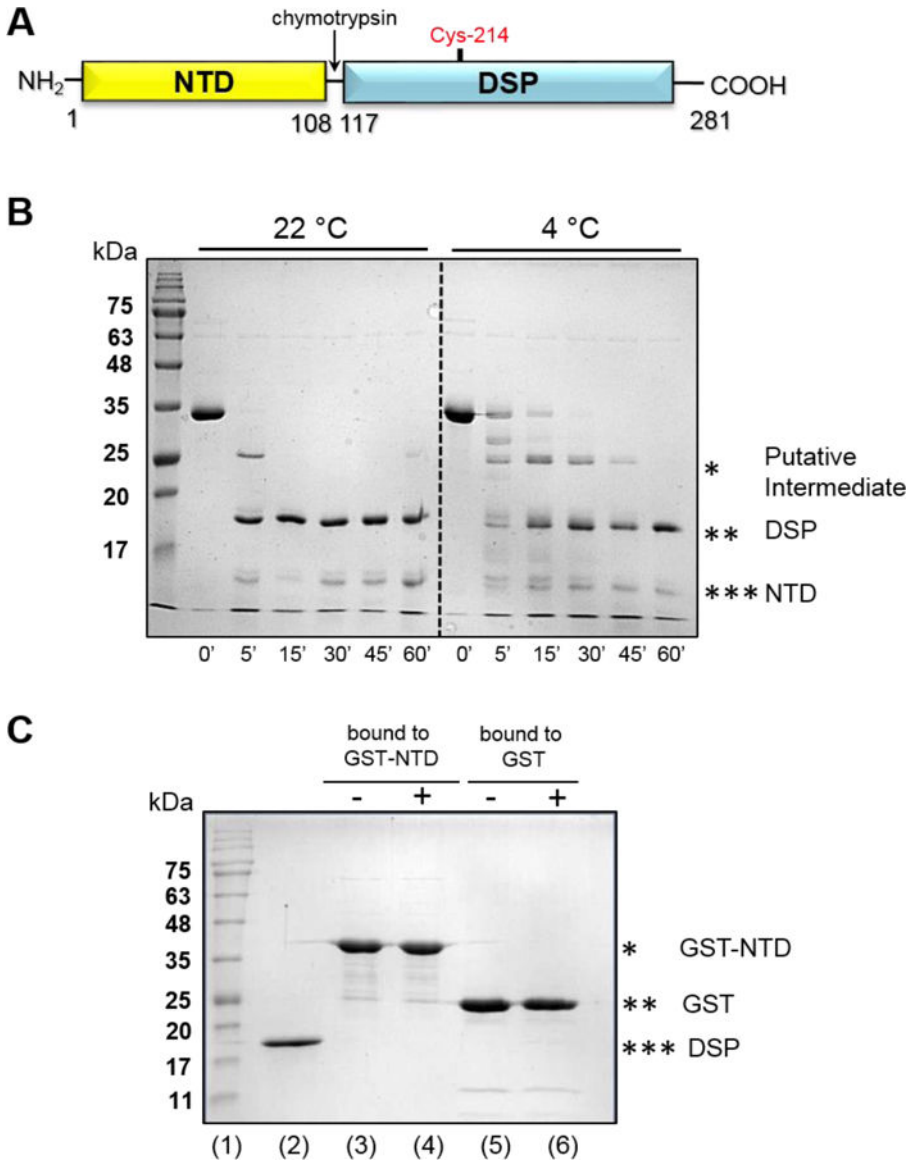

Figure 1. ***Saccharomyces cerevisiae*** **Siw14.**

(**A**) Schematic diagram of Siw14 domain organization. (**B**) Limited proteolysis analysis of FL-Siw14 in the presence of chymotrypsin at 22° C and 4° C. Aliquots of the digestion reaction were collected after 5, 15, 30, 45 and 60 minutes and resolved by 12.5% SDS-PAGE. (**C**) Pull down analysis of Siw14-DSP (lane 2) binding to GST-NTD (lane 3,4) or free GST (lane 5,6) coupled to glutathione beads. In lanes 4 and 6 are fractions bound to beads. All samples were analyzed by 12.5% SDS-PAGE.

Author Manuscript Author Manuscript Author Manuscript Author Manuscript

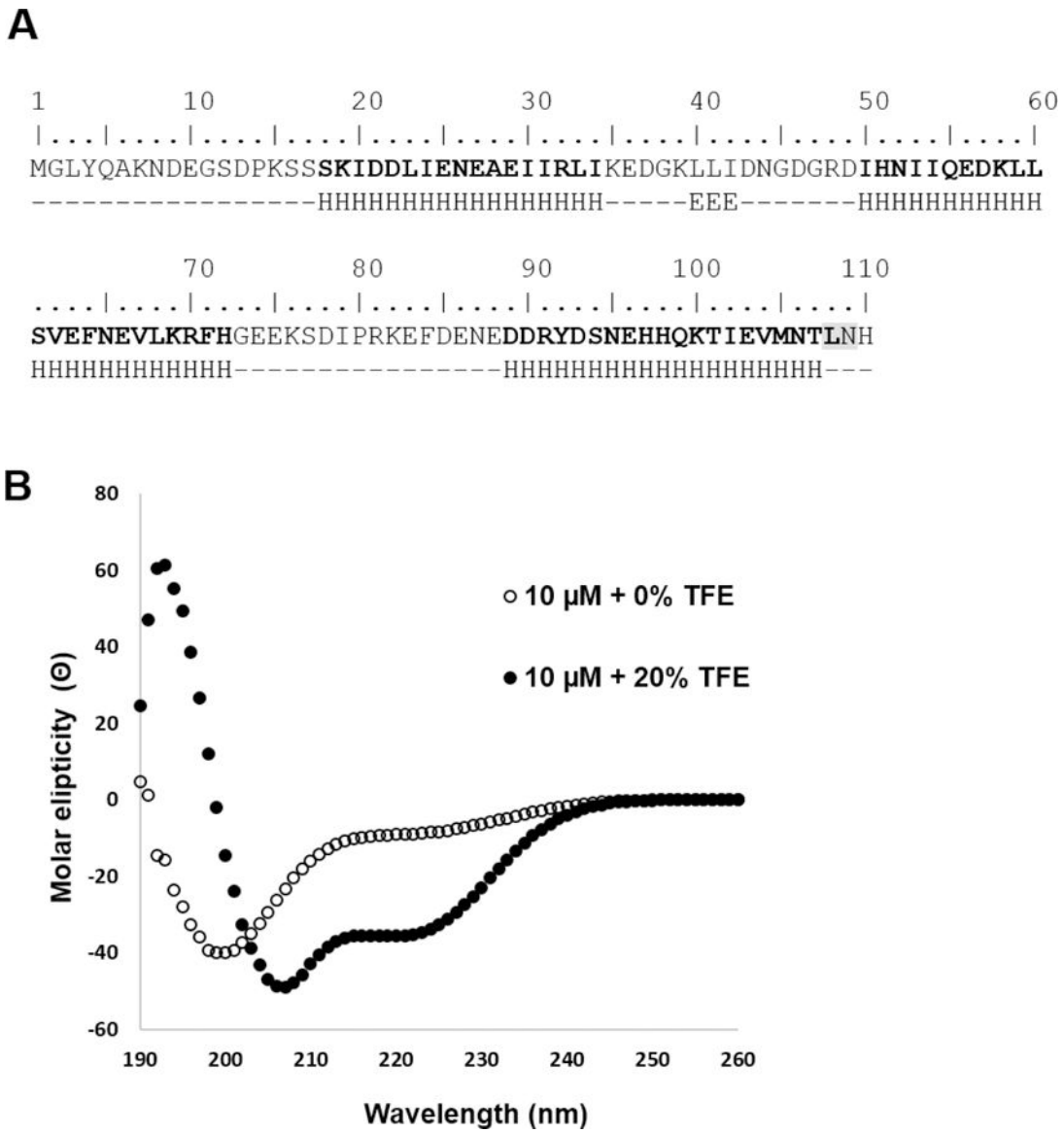

Figure 2. Siw14-NTD is enriched in α-helices.

(**A**) The amino acid sequence of Siw14-NTD and secondary structure content predicted by Jpred4 (45). Bolded residues correspond to regions predicted to fold as α-helices (H); random coil and β-strands are indicated by (–) and (E), respectively. The gray box indicates the site of chymotrypsin cleavage. (**B**) *Far*-UV CD spectrum of 10 μM Siw14-NTD at pH 7.4 in the presence (●) and absence (○) of 20% TFE.

Author Manuscript Author Manuscript Author Manuscript Author Manuscript

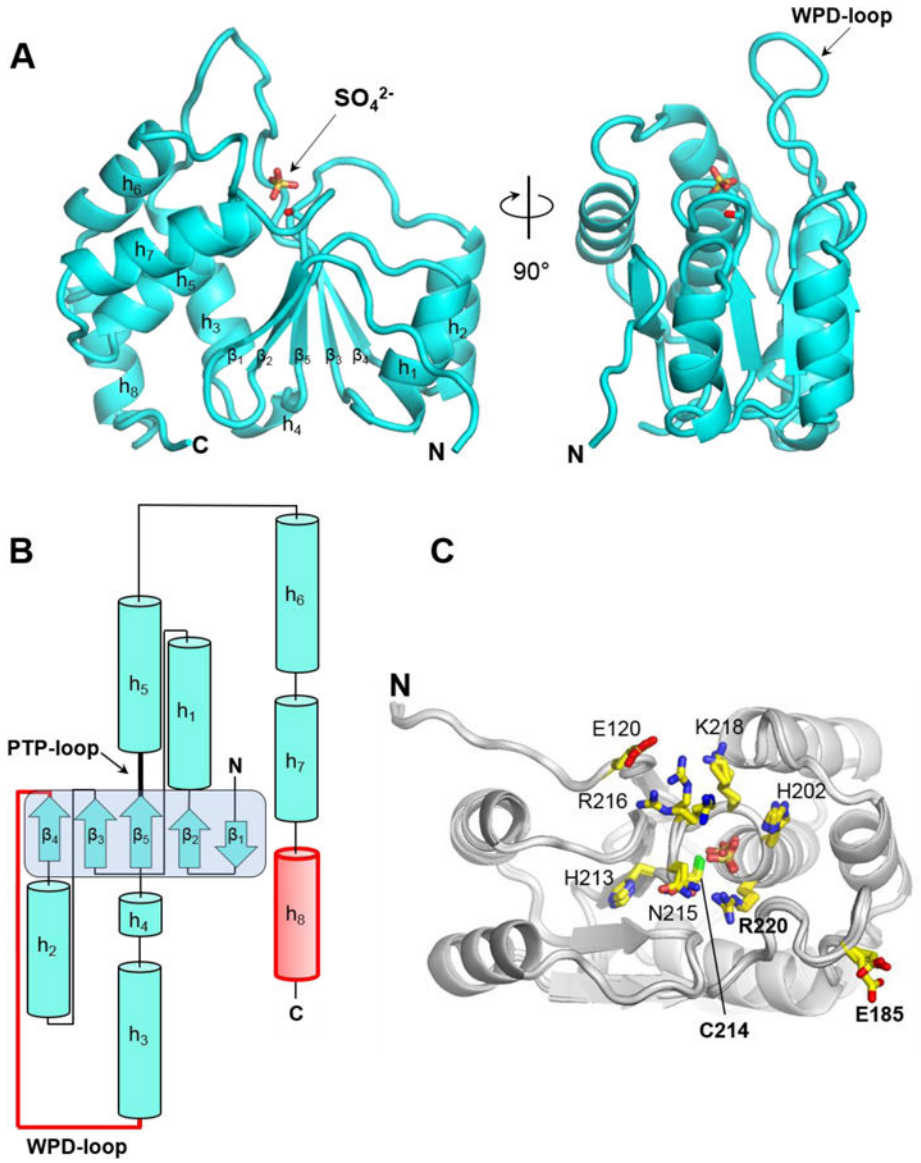

Figure 3. Crystal structure of Siw14-DSP.

(**A**) Ribbon diagram of Siw14-DSP with Cys-214 shown as a red stick. The active site sulfate is in yellow and red. (**B**) Topological diagram of Siw14-DSP; the central β-sheet formed by strands β_1-β_5 is highlighted in light blue. The WPD-loop and α-helix h_8 not found in laforin are colored in red. (**C**) Conformation of the Siw14 PTP-binding loop. Superimposition of three representative Siw14-DSP chains found in the ASU viewed from the top. Critical residues in the PTP-loop, as well as Glu-120 and Glu-185 and the active site sulfate ions, are shown as sticks.

Author Manuscript Author Manuscript Author Manuscript Author Manuscript

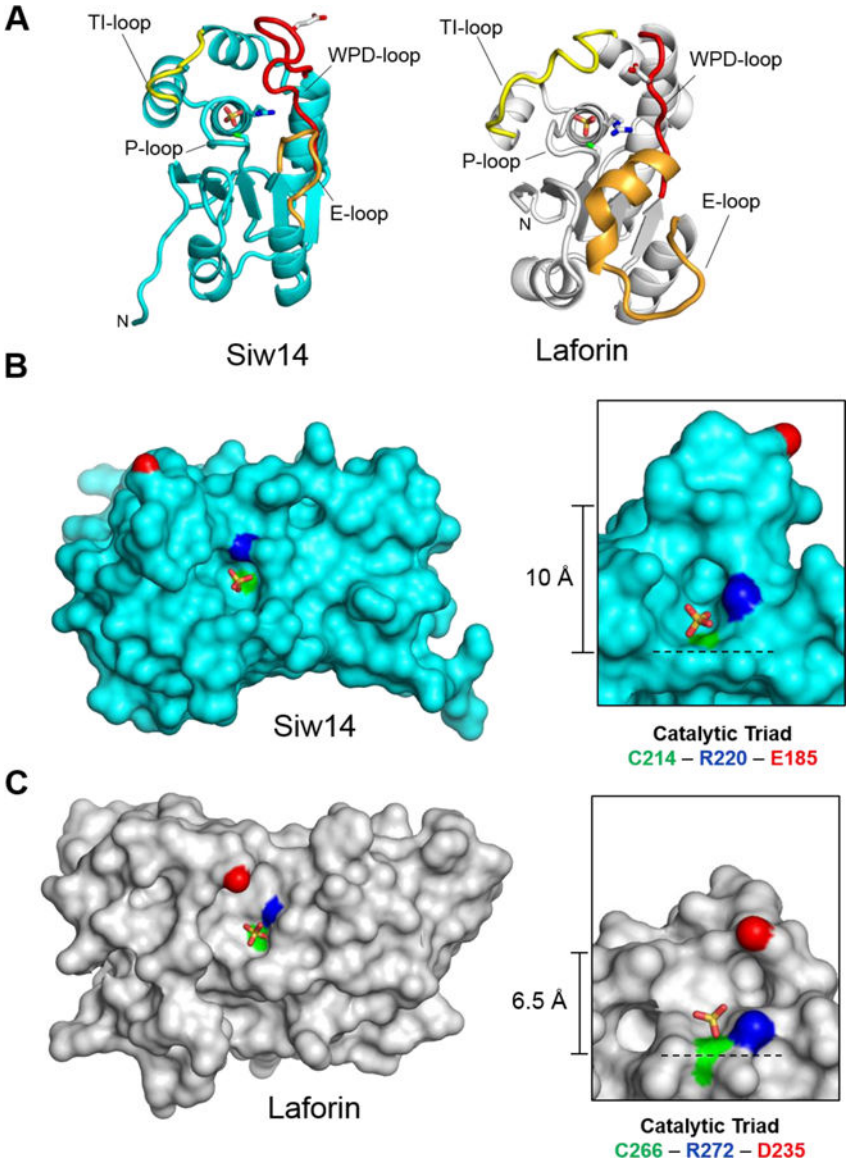

Figure 4. Comparing DSP domains: Siw14 *versus* laforin.

(**A**) Top views of the Siw14-DSP (left) and laf-DSP (right) (PDB 4R30) highlighting critical loops surrounding the active site. Surface representation of (**B**) Siw14-DSP and (**C**) laf-DSP. In both panels, the catalytic triads Cys-214/Cys-266, Arg-220/Arg-272 and Glu-185/Asp-235 are colored in green, blue and red, respectively. Next to each panel is a magnified cut-through view of the catalytic pocket revealing differences in the depth of the active site crevice. The dashed line indicates the floor of the active site crevice.

Author Manuscript Author Manuscript Author Manuscript Author Manuscript

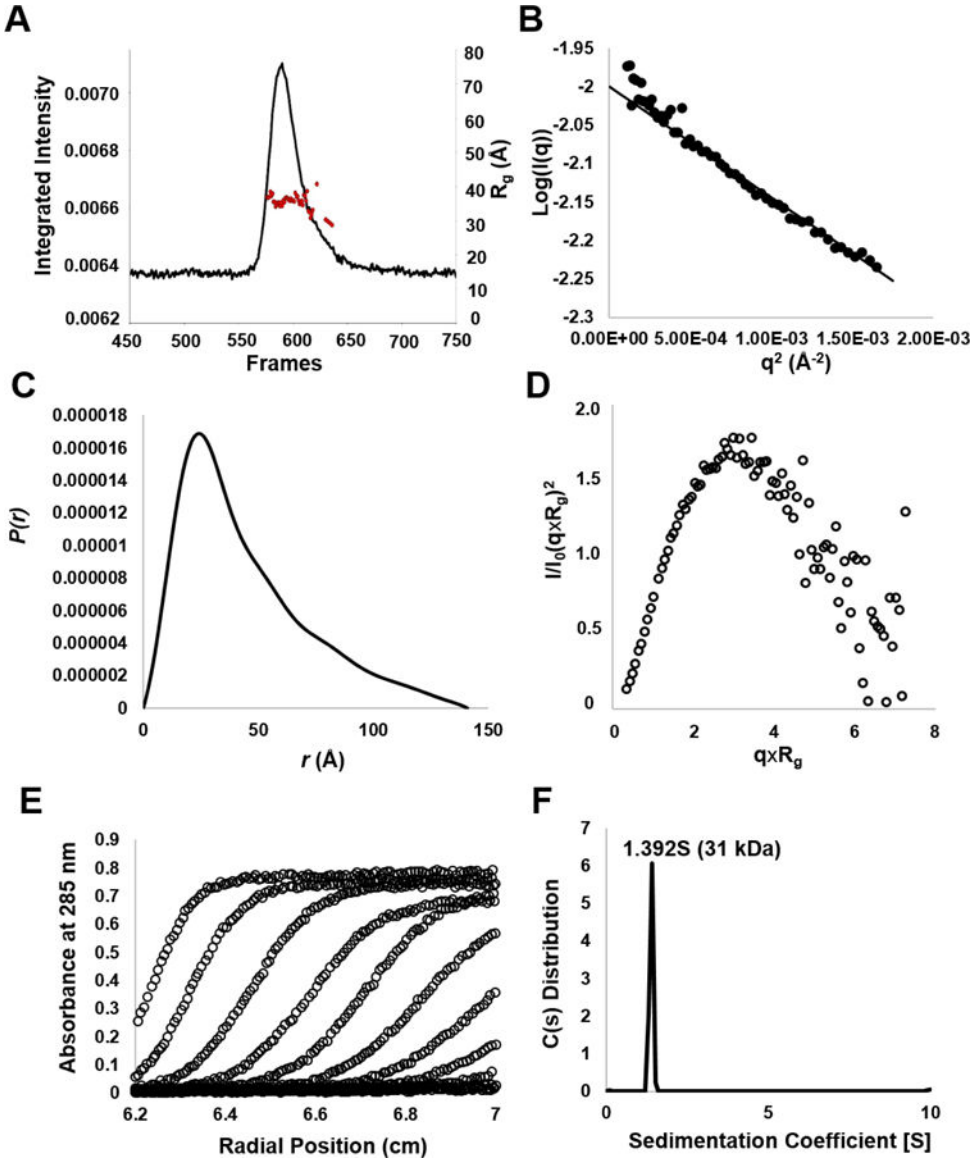

Figure 5. In solution biophysical characterization of FL-Siw14.

(**A**) SEC-SAXS profile of FL-Siw14 at 7.2 mg ml^{-1} measured in 20 mM Tris-HCl pH 8.0, 0.15 M NaCl, and 5 mM β-Mercaptoethanol at 4 °C. The red dots indicate R_g values (on the y-axis) corresponding to frames (X-axis). (**B**) Guinier plots calculated from averaging buffer-subtracted scattering intensities from frames both before (469–525) and after (762–862) the sample peak (575–613). The coefficient of determination, R^2 is 0.9785. (**C**) *P(r)* function (**D**) and normalized *Kratky* plot calculated from SEC-SAXS data. (**E**) Sedimentation velocity profiles of FL-Siw14 at 1.7 mg ml^{-1} measured in 0.15 M NaCl at 4 °C. Raw absorbance at 285 nm plotted as a function of the radial position. Data at intervals of 80 min are shown as dots for sedimentation at 50,000 rpm. (**F**) Fitted distribution of the apparent sedimentation coefficient (s*) calculated for FL-Siw14 is 1.39S (and s20, w=1.46S) corresponds to an estimated molecular mass of ~31.0 kDa, consistent with a monomer. A list of SEC-SAXS and hydrodynamic parameters are in Table 2.

Author Manuscript Author Manuscript Author Manuscript Author Manuscript

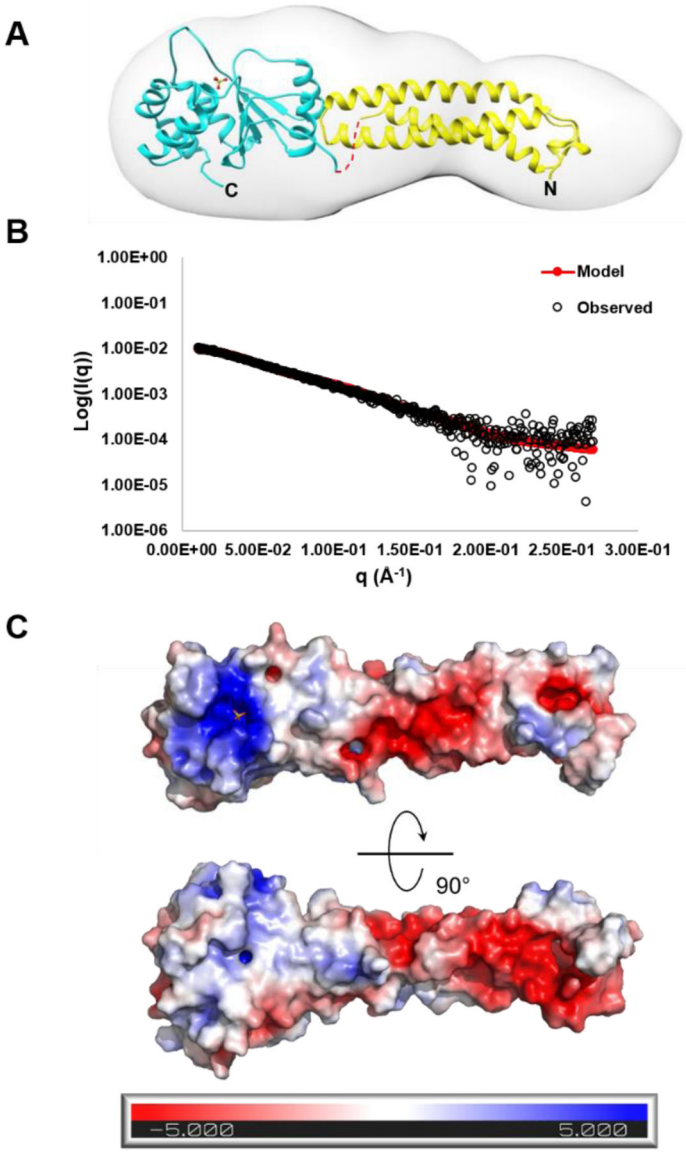

Figure 6. A complete *pseudo*-atomic model of FL-Siw14.

(**A**) *Ab initio* SEC-SAXS electron density of FL-Siw14. The crystallographic structure of Siw14-DSP and *de novo* model of Siw14-NTD are docked inside the SAXS density. The chymotrypsin-susceptible linker is shown as a dashed red line. (**B**) Overlay of the experimental SEC-SAXS data for FL-Siw14 (blue circles) and scattering data calculated from the *pseudo*-atomic model in panel A (red line). The χ^2 value calculated by the FoXS server (43) is 1.7. The corresponding *P(r)* functions are shown in Fig. 5C. (**C**) The electrostatic surface potential of FL-Siw14 *pseudo*-atomic model reveals significant charge difference between NTD and DSP. The charge scale from APBS (51) is between −5 kT/e representing region of negative charges (colored in red) and +5 kT/e representing region of positive charges (colored in blue).

Author Manuscript Author Manuscript Author Manuscript Author Manuscript

Table 1.

Crystallographic data collection and refinement statistics

	Siw14-DSP
Data collection	
Beamline	SSRL 9–2
Wavelength (Å)	0.972
Space group	C2
Cell dimensions	
a, *b*, *c* (Å)	92.5, 160.5, 360.6
α, *β*, *γ* (°)	90.0, 90.3, 90.0
Reflections (tot/unique)	1,839,305 / 166,746
Resolution (Å)	50.0–2.5 (2.59–2.5)
Completeness (%)	91.3 (83.1)
Redundancy	2.3 (2.0)
R_{sym}	13.5 (78.8)
R_{pim}	10.5 (60.9)
I / σ_I	11.5 (1.9)
Wilson B factor (Å^2)	37.4
Refinement	
PDB entry	**6E3B**
Resolution limits (Å)	15.0–2.50
No. of reflections ($\|F_{obs}\|\sigma_{Fobs}>2$)	163,094
R_{work} / R_{free} [a]	22.98 / 24.63
No. of protein atoms	33,542
No. of solvent molecules	382
No. of sulfate ions	24
B-factor (Å^2)	
Protein atoms	55.8
Sulfate ions	47.7
Waters	34.3
Ramachandran plot (%)	
core/allow/gen. allow/disallowed	93.81/6.09/0.10
Rms deviations from ideal	
Bond lengths (Å)	0.005
Bond angles (°)	1.00
MolProbity score / Clash score	1.97 / 10.92

[*] Values in parentheses are for the highest-resolution shell.

[a] The R_{free} value was calculated using ~2,000 reflections selected in 20 thin resolution shells.

Author Manuscript Author Manuscript Author Manuscript Author Manuscript

Table 2.

Biophysical parameters measured using AUC and SAXS

SEC-SAXS	**FL-Siw14**
Instrument	G1-beamline
Wavelength (Å)	1.25
Exposure time (s)	1
Protein Concentration (mg ml^{-1})	7.2
Temperature (K)	277
Radius of Gyration, R_g * (Å)	33.3 + 0.3
Maximum Diameter, D_{max}	141
Porod M.W. ** / Theoretical M.W. (kDa)	34.2 / 32.7
Software employed	
Primary Data Reduction	RAW
Data Processing	ATSAS
Ab initio analysis	DENSS
Validation and averaging	EMAN2
Rigid-body refinement	Phenix.real_space_refine
Computation of model intensities	FoxS
3D-graphics representations	PyMOL
AUC-SV	
Protein Concentration (mg ml^{-1})	1.7
Apparent Sedimentation Coef., s (S)	1.39
Absolute Sedimentation Coef., $s_{20,w}$ (S)	1.46
Estimated / Theoretical M.W. (kDa)	31.0 / 32.7
Frictional Ratio, f/f_0	2.5
Radius of Hydration, R_H (Å)	30.0

*Rg was determined from Guinier plot.

**Porod M.W. is calculated as the Porod volume (A^3) / 1.8.